npj | 2D materials and applications

Article

Published in partnership with FCT NOVA with the support of E-MRS

https://doi.org/10.1038/s41699-024-00459-8

Inducing room-temperature valley polarization of excitonic emission in transition metal dichalcogenide monolayers

Sergii Morozov [1] ✉, Torgom Yezekyan[1,2], Christian Wolff[1], Sergey I. Bozhevolnyi[2,3] & N. Asger Mortensen [1,3]

The lowest energy states in transition metal dichalcogenide (TMD) monolayers follow valley selection rules, which have attracted vast interest due to the possibility of encoding and processing of quantum information. However, these quantum states are strongly affected by temperature-dependent intervalley scattering leading to complete valley depolarization, which hampers practical applications at room temperature. Therefore, for achieving clear and robust valley polarization in TMD monolayers one needs to suppress parasitic depolarization processes, which is the central challenge in the growing field of valleytronics. Here, in electron-doping experiments on TMD monolayers, we show that strong doping levels beyond 10^{13} cm^{-2} can induce 61% and 37% valley contrast at room temperature in tungsten diselenide and molybdenum diselenide monolayers, respectively. Our findings demonstrate that charged excitons in TMD monolayers hold the potential for the development of efficient valleytronic devices functional at 300 K.

The ultimate thickness of transition metal dichalcogenide (TMD) monolayers and the convenient access to valley degrees of freedom are inspiring features for the next-generation electronic and optoelectronic devices[1]. Such valleytronic devices utilize the possibility to create imbalanced carrier populations in K and K′ energy extrema (valleys) of the Brillouin zone by optical pumping[2–4]. However, valley depolarization processes may equilibrate the desired carrier population imbalance between K and K′ valleys, resulting in loss of intended functionality in a valleytronic device. Therefore, the control of parasitic depolarization processes is essential for unlocking the full power of valleytronics.

Valley polarization in TMD monolayers has been shown to be sensitive to temperature, magnetic field, mechanical strain, charge doping, etc.[3–8]. While cryogenic temperatures can suppress phonon-assisted valley depolarization processes[3], such conditions are impractical for real-life applications at ambient conditions. Besides, cryogenic conditions are not a comprehensive remedy against other valley depolarization mechanisms, as in the case of molybdenum diselenide monolayers, which exhibit near-zero valley contrast even at 4 K[9]. To induce a high degree of valley polarization (DVP), the radiative relaxation processes with characteristic time τ_r should be faster than the valley depolarization time τ_v, i.e., their ratio should be minimal in the phenomenological expression[2]

$$\mathrm{DVP} = \frac{P_0}{1 + \tau_r/\tau_v}, \tag{1}$$

where $P_0 \leq 1$ is the initial laser-induced degree of polarization depending on the sample quality and environment. High valley polarization at room temperature has been achieved through manipulation of τ_r (relative to τ_v) by enhancing the emission rates with optical antennas[10,11] or by introducing nonradiative recombination pathways in graphene-TMD heterostructures[12]. A complementary approach relies on the screening effect of the electron-hole exchange interaction due to charge doping[7,13,14], which in chalcogenide-alloyed monolayer hybrids allowed for a very high valley polarization of 50% at room temperature[15]. Similarly, direct electrostatic and optical doping techniques were demonstrated to enhance the valley polarization at low temperatures[5,16]. However, such doping

[1]POLIMA—Center for Polariton-driven Light–Matter Interactions, University of Southern Denmark, Campusvej 55, DK-5230 Odense M, Denmark. [2]Center for Nano Optics, University of Southern Denmark, Campusvej 55, DK-5230 Odense M, Denmark. [3]Danish Institute for Advanced Study, University of Southern Denmark, Campusvej 55, DK-5230 Odense M, Denmark. ✉e-mail: semo@mci.sdu.dk

techniques do not provide sufficient doping levels to enable practical valley contrast at room temperature.

In this article, we demonstrate strong valley polarization of excitonic emission in electrochemically–doped TMD monolayers at room temperature. We achieve 61% and 37% valley contrast in tungsten diselenide (WSe_2) and molybdenum diselenide ($MoSe_2$) monolayers at high electron doping densities $>10^{13}$ cm^{-2}, respectively. We investigate the effect of electron doping on the characteristic emission and intervalley scattering times, which provides control over the valley depolarization dynamics. Our results pave the way for designing of practical valleytronic devices operating at room temperature.

Results

Samples and experimental setup

We mechanically exfoliated WSe_2 and $MoSe_2$ bulk crystals into monolayers —see details in Supplementary Methods and Supplementary Fig. 1. All experiments presented here were performed at room temperature of ca. 293 K. Representative photoluminescence spectra of exfoliated monolayers at low excitation power are shown in Fig. 1a, b. Here, we use the spectral decomposition fitting with a three-peak Voigt function to distinguish contributions of the neutral exciton X_0 (orange) and negative trion X_T (purple) emission[17]. The third low-intensity peak X_D (gray) is not of interest here and possibly, originates from recombination through defect and impurity states. We extract spectral parameters for X_0 and X_T peak energies as well as their linewidth at half-intensity (Table 1).

We position the TMD monolayers in contact with an indium tin oxide (ITO) substrate (see the inset of Fig. 1c), which serves as a working electrode of our custom-made electrochemical cell (see details in Supplementary Methods and Supplementary Fig. 2). Additionally, our monolayers are covered with hexagonal boron nitride (hBN) crystals for protecting them from direct Faradaic currents as well as the photochemical degradation due to the chemically-active electrolyte environment[17]. For the polarization measurements, the samples are tested with a right-handed circularly polarized (σ_+) laser at off- and near-resonance energies (1.58, 1.70, and 1.81 eV). Generated photoluminescence is analyzed with a polarization-resolving microscopy setup (Fig. 1c, see details in Supplementary Methods), which allows for simultaneous detection of co- (σ_+/σ_+) and cross-polarized (σ_+/σ_-) emission on a charge-coupled device (CCD) camera of a spectrometer. The application of voltage bias in the electrochemical cell controls the position of the Fermi level E_F in the TMD monolayer. At the neutral voltage bias of 0 V, E_F is within the bandgap as in the case of an intrinsic monolayer (Fig. 1d), while a negative bias can raise E_F above the bottom of the conduction band, causing electron doping and filling of available states in the K and K′ valleys of the Brillouin zone (Fig. 1e).

Optical doping

First, we present the response of valley polarization to exciton charging using the optical doping technique (photocharging)[5]. High laser power (pump fluency) facilitates the formation of charged excitons (trions), increasing their contribution in the photoluminescence signal (see Supplementary Fig. 3). Here, we use right circularly polarized lasers at non-resonant energies of $E_{exc} = 1.81$ eV and 1.70 eV to excite the WSe_2 and $MoSe_2$ monolayers, respectively.

Figure 2a, b presents polarization-resolved photoluminescence spectra of WSe_2 and $MoSe_2$ monolayers measured at high excitation power of >1 kW cm^{-2}, where the green and blue lines represent the co- and cross-polarized detection channels. We employ the spectra decomposition fit (red), extracting X_0 (orange) and X_T (purple) peaks with respect to the polarization (solid and dashed lines for the co- and cross-polarized spectra). We observe a slight valley polarization in the emission of the WSe_2 monolayer at high excitation power (Fig. 2a, c), while the $MoSe_2$ monolayer exhibits no valley polarization regardless of excitation power (Fig. 2b, d). We quantify this in Fig. 2c, d (blue line) by the degree of circular polarization—$DOCP = (I_{\sigma_+} - I_{\sigma_-})/(I_{\sigma_+} + I_{\sigma_-})$—using the spectra from Fig. 2a, b, respectively. In comparison, the yellow line in Fig. 2c, d represents a DOCP obtained at low excitation power. The increase of excitation power to 9.2 kW cm^{-2} results in a growth of DOCP around the trion spectral line up to 9% in the WSe_2 monolayer, which we attribute to the optical charge doping. We repeat the experiment on a different WSe_2 monolayer with a higher trion contribution to the signal (Supplementary Fig. 3), however obtaining similar low values of valley polarization contrast. This demonstrates the limitations of the optical doping approach to achieve a high valley polarization at room temperature, while a further increase of excitation power may cause unwanted heating of the sample, parasitic defect and substrate emission, flourishing nonlinear processes, as well as irreversible photodegradation of a TMD monolayer.

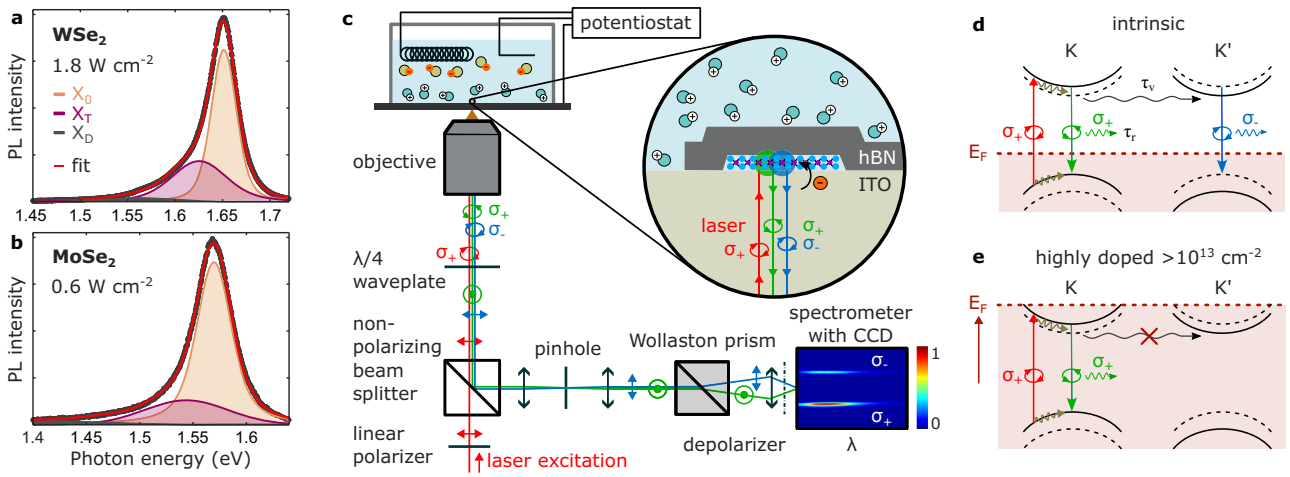

Fig. 1 | Charging excitons in an electrochemical cell. a, **b** Photoluminescence spectra of WSe_2 and $MoSe_2$ monolayers at low laser power. The monolayers are sandwiched between an ITO substrate and a multilayer hBN flake. The orange and purple peaks represent the contribution of neutral exciton X_0 and trion X_T, respectively, which are obtained by the spectral decomposition fit (red). **c** Experimental setup for electron doping and polarization-sensitive detection of valley photoluminescence (see Supplementary Methods for details). **d** Schematic band structure of a TMD monolayer around K and K′ points of the Brillouin zone. The red dashed line represents the Fermi level E_F, which for an intrinsic monolayer, lies within the bandgap. The wavy gray arrow represents the intervalley scattering processes, and the green and blue arrows—radiative recombination generating right- (σ_+) or left-handed (σ_-) circularly polarized photons, respectively. **e** Application of a negative voltage bias in the electrochemical cell rises E_F above the bottom of the conduction band causing strong electron doping, which leads to the suppression of intervalley scattering processes and parasitic cross-polarized photoluminescence.

Table 1 | Photoluminescence of WSe_2 and $MoSe_2$ monolayers

	E_{X_0} (eV)	δE_{X_0} (meV)	E_{X_T} (eV)	δE_{X_T} (meV)
WSe_2	1.670	35	1.622	64
$MoSe_2$	1.570	41	1.543	118

Results of spectral decomposition for peak energies of neutral exciton E_{X_0} and trion E_{X_T}, and their linewidth at half-intensity $\delta E_{X_0,T}$.

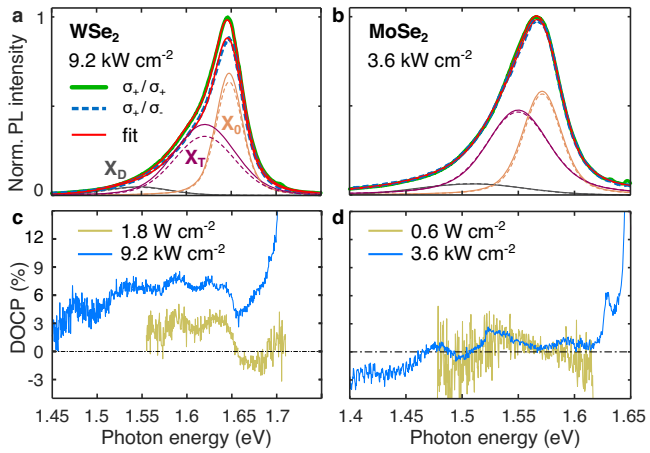

Fig. 2 | Valley-resolved photoluminescence in optically doped TMD monolayers. **a**, **b** At high laser power of >1 kW cm^{-2}, the WSe_2 monolayer exhibits slight valley polarization of up to 9%, while the $MoSe_2$ monolayer remains unpolarized. The orange and purple peaks represent the neutral exciton X_0 and trion X_T contributions extracted from spectral fits (red solid lines). The solid and dashed lines correspond to the co- (σ_+/σ_+) and cross-polarized (σ_+/σ_-) detection channels. **c**, **d** Degree of circular polarization measured at low (yellow) and high (blue) excitation powers.

We conclude here that the valley polarization in a WSe_2 monolayer (Fig. 2a, c) mainly originates from the trion emission, which is in agreement with previous studies[5,18,19]. In contrast, a $MoSe_2$ monolayer exhibits no valley polarization in the X_0 and X_T spectral regions at low and high excitation powers, highlighting the material difference between the TMD monolayers. We also test our samples with a linearly polarized laser observing a near-zero degree of linear polarization (DOLP) in the X_T spectral region (Supplementary Fig. 4), which is also independent of the excitation power. A linearly polarized excitation can generate quantum coherent valley states of the neutral exciton[4]. However, we note that the detection of trion quantum coherence cannot be accessed in such an experiment and requires complementary experimental techniques[20].

Electrochemical doping

We now turn to discuss the manipulation of TMD monolayer photoluminescence via electrochemical doping. The evolution of photoluminescence intensities from WSe_2 and $MoSe_2$ monolayers during a linear scan of voltage bias are shown in Supplementary Fig. 5, where at negative bias, the photoluminescence experiences a substantial drop in intensity. To characterize the change, we perform the spectral decomposition fitting, extracting the intensity evolution of the neutral exciton X_0 at negative bias (Fig. 3a, b). The X_0 intensity suppression dynamics follow the Fermi-Dirac distribution $f(E) = [\exp(-E/k_BT) + 1]^{-1}$ at room temperature as $I(E_F) = I_0 \cdot [1 - f(E_F)]$ (red in Fig. 3a, b), which we demonstrated in our previous work[17]. This model of exciton intensity dynamics allows us to translate the applied voltage bias to the Fermi energy with respect to the bottom of the conduction band, as well as to the electron doping density (see details in Supplementary Methods). Here, $[1 - f]$ is the common Pauli blocking factor describing the probability that the state is empty, allowing for the possibility of an exciton being formed when an electron transitions from the valence band. The decrease of photoluminescence intensity at negative bias arises from the filling of the monolayer conduction band with electrons, which redistributes the oscillator strength between neutral exciton and trion excitations[21]. On one hand, this suppresses the neutral exciton contribution in photoluminescence and favors trion formation, while, on the other one, leaves fewer states for intervalley transitions preventing the depolarization.

Figure 3c, d summarizes the spectral response to negative bias. The insets of Fig. 3c, d shows photoluminescence spectra obtained at neutral and negative bias, demonstrating a substantial change in the emission energy. This is in line with our previous work[17], where we showed that the change in spectrum is due to the suppression of neutral exciton and generation of trion emission at large doping densities. Besides, the trion emission energies of both WSe_2 and $MoSe_2$ start to redshift linearly once the Fermi level passes the bottom of the conduction band. We measure a maximal redshift in WSe_2 and $MoSe_2$ monolayers of 73 meV and 104 meV at −1.6 V and −0.8 V, respectively, which corresponds to electron doping density of 26×10^{12} cm^{-2} and 48×10^{12} cm^{-2}.

The suppression of X_0 intensity (Fig. 3a, b) and the redshift in emission spectra (Fig. 3c, d) at negative bias are accompanied by a reduction of experimental emission lifetime τ_r (Fig. 3e, f). We note here that the reported experimental lifetimes do not represent the intrinsic exciton decay rate in the TMD monolayers but instead are effective radiative lifetimes that depend on a number of different factors[22]. The insets of Fig. 3e, f show decay histograms measured at neutral and negative bias, which we fit with a bi-exponential decay function to extract values of the experimental lifetime (Supplementary Fig. 6). We attribute the fast decay component to the primary excitonic recombination channel as it has a dominant weight in the fit and plot its devolution with negative bias in Fig. 3e, f. The slow decay component may originate from defect-assisted or phonon-mediated recombination processes, while an accurate interpretation of experimentally measured lifetimes poses a complex challenge, particularly at room temperature[22]. Here, we observe a major enhancement of the radiative recombination rate (the quantitative estimation is beyond the resolution of our system of ca. 180 ps, gray-shaded region in Fig. 3e, f), when the Fermi level crosses the bottom of the conduction band. Similar to the case of the suppression of photoluminescence intensity in Fig. 3a, b, we model the radiative lifetime dynamics at increasing electron doping with the Fermi-Dirac distribution

$$\tau_r(E_F) = \tau_{r,0} \cdot [1 - f(E_F)], \quad (2)$$

where $\tau_{r,0}$ is the lifetime at 0 V bias (red curve in Fig. 3e, f). We note here again the difference in the response of WSe_2 and $MoSe_2$ monolayers: while the redshift in spectra and the lifetime reduction happens for WSe_2 around zero Fermi energy in Fig. 3c, e, the response of $MoSe_2$ is shifted to higher Fermi energies in Fig. 3d, f.

The reduction in experimental radiative lifetime τ_r mainly stems from two processes: (i) formation of trions with faster recombination times τ_T, and (ii) increasing probability of non-radiative Auger-related recombination characterized by τ_{nr}[18], that is $\tau_r^{-1} = \tau_T^{-1} + \tau_{nr}^{-1}$ in the spirit of Matthiessen's rule. We speculate that the strong electron doping enhances the radiative decay of excitonic emission, and if it is faster than the characteristic time of intervalley scattering processes at room temperature—it can induce the sought-after valley polarization contrast.

Valley-polarization at strong electron doping

Finally, we characterize valley polarization properties of WSe_2 and $MoSe_2$ monolayers at the negative bias voltages (laser power <1 kW cm^{-2}), which shift the Fermi level well above the bottom of the conduction band. Photoluminescence of WSe_2 and $MoSe_2$ monolayers at neutral bias of 0 V are characterized by a low DOCP (black curves in Fig. 4c, d, Supplementary Fig. 7), which are similar to what has been observed in the optical doping experiments (Fig. 2). In contrast, Fig. 4a, b present strongly polarized spectra of WSe_2 and $MoSe_2$ monolayers obtained at high negative bias with

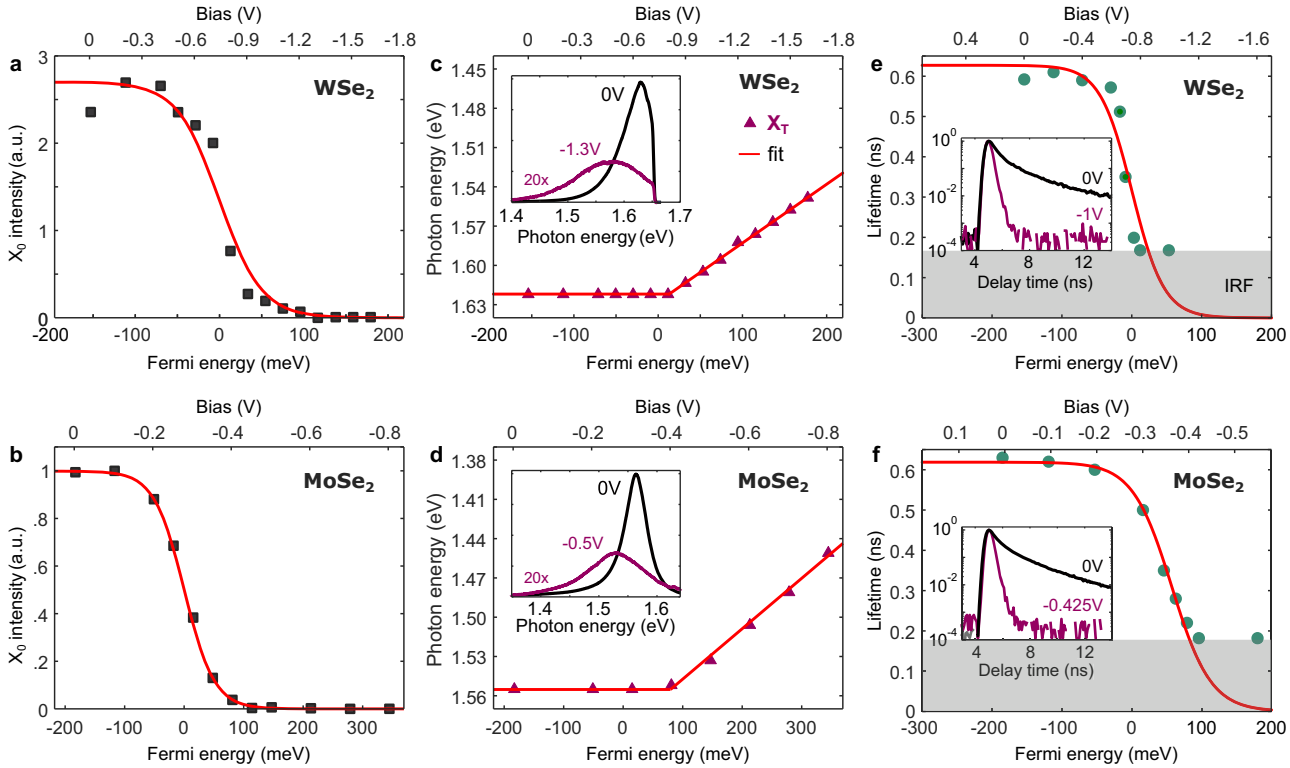

Fig. 3 | Photoluminescence in strongly doped TMD monolayers. a, **b** Intensity response of neutral exciton X_0 (black squares) to negative bias follows the Fermi-Dirac distribution (red). **c**, **d** Linear redshift of negative trion X_T emission maximum (purple triangles) for Fermi levels above the bottom of the conduction band. The insets show emission spectra at neutral (black) and negative (purple) bias, both monolayers are excited with a laser at 1.70 eV. **e**, **f** The reduction in radiative lifetime under negative bias (circles) aligns with the Fermi-Dirac distribution (red). The insets show decay histograms at neutral (black) and negative (purple) bias. The gray-shaded area represents the lifetime of the experimental limit—instrument response function (IRF).

dominating trion emission. To quantify the trion valley polarization contrast, we employ the spectrum decomposition fit, extracting X_T intensities in co- ($I^T_{\sigma_+}$) and cross-polarized ($I^T_{\sigma_-}$) spectra to calculate the experimental DVP of X_T via $(I^T_{\sigma_+} - I^T_{\sigma_-})/(I^T_{\sigma_+} + I^T_{\sigma_-})$. The purple-shaded areas in Fig. 4a, b present the extracted trion intensity contributions $I^T_{\sigma_+}$ and $I^T_{\sigma_-}$ to the spectra with respect to the polarization, which we used to calculate the experimental trion DVP of 48% and 36% for WSe_2 and $MoSe_2$ monolayers at the given voltage bias and laser energy, respectively. Furthermore, we test the polarization response to the excitation energy (Fig. 4c, d, Supplementary Fig. 8), where the DOCP significantly increases for near-resonant excitation of the TMD monolayers.

The dynamics of trion polarization at increasing negative bias are presented in Fig. 4e, f. Here, we measure spectra in a wide range of negative biases to extract the trion DVP as a function of bias (top scale) and Fermi energy (bottom scale). Besides, the trion polarization dynamics follow a similar trend at off- and near-resonant laser excitation, experiencing a transition to strong valley polarization once the Fermi level is shifted above the bottom of the conduction band (see also sample-to-sample variations in Supplementary Fig. 9). We fit the transition to high valley polarization using Eq. (1) (red in Fig. 4e, f), where we introduce a dependency on the Fermi energy for both characteristic lifetimes, i.e.,

$$\mathrm{DVP}(E_F) = \frac{P_0}{1 + \tau_r(E_F)/\tau_v(E_F)}. \quad (3)$$

For the radiative lifetime τ_r dependency on E_F we use Eq. (2), while the valley depolarization time τ_v in the case of statically screened Coulomb potential with finite Thomas–Fermi wave vector can be expressed as[13–15]

$$\tau_v(E_F) = \tau_{v,0} \cdot [1 - \exp(-E_F/k_B T)]^2, \quad (4)$$

where $\tau_{v,0}$ is the valley depolarization time at zero temperature, thus having the $\tau_{r,0}/\tau_{v,0}$ ratio as the only fitting parameter. The fits of trion DVP in Fig. 4e, f (red) saturate in the strong-doping regime of $E_F > 100$ meV ($>10^{13}$ cm^{-2}), and for the near-resonant excitation reach 61% and 37% for WSe_2 and $MoSe_2$ monolayers, respectively. We note here that the sole dependency of τ_v on E_F in Eq. (3) is not sufficient to unambiguously fit our experimental results in Fig. 4e, f (Supplementary Fig. 10), which highlights the importance of developing a more accurate model for the emission lifetime $\tau_r(E_F)$ reduction accounting for many-body interactions at high electron concentrations. Besides, our simple model does not take into account the intervalley lifetime dependence on the temperature-dependent excitonic linewidth[14]. We note that the lower DVP in the $MoSe_2$ monolayer, in comparison with that of the WSe_2 one, is expected for the wider trion linewidth (as reported in Table 1), which also indicates poorer coherence times in $MoSe_2$ monolayers. We suggest that strain engineering can be employed for narrowing of linewidth[8], which can improve coherence times and further increase the DVP at room temperature.

Discussion

We compare our results with literature DVP at cryogenic and room temperature conditions in Fig. 5. Here, we plot DVP values for a range of TMD monolayers as well as their chalcogenide-alloyed hybrids. With values of 61% for WSe_2 and 37% for $MoSe_2$, we observe the highest valley polarization contrast to date at room temperature, which emphasizes the importance of the strong doping regime for achieving a high DVP at ambient conditions. Our experiments reveal a difference between the DVP attainable in WSe_2 and $MoSe_2$ monolayers, which highlights the role of careful material selection for the further improvement of valley contrast.

Implementing strong electron doping in TMD monolayers for practical use might face challenges. Replacing the liquid electrolyte with a solid-state one could improve device robustness and versatility. Additionally,

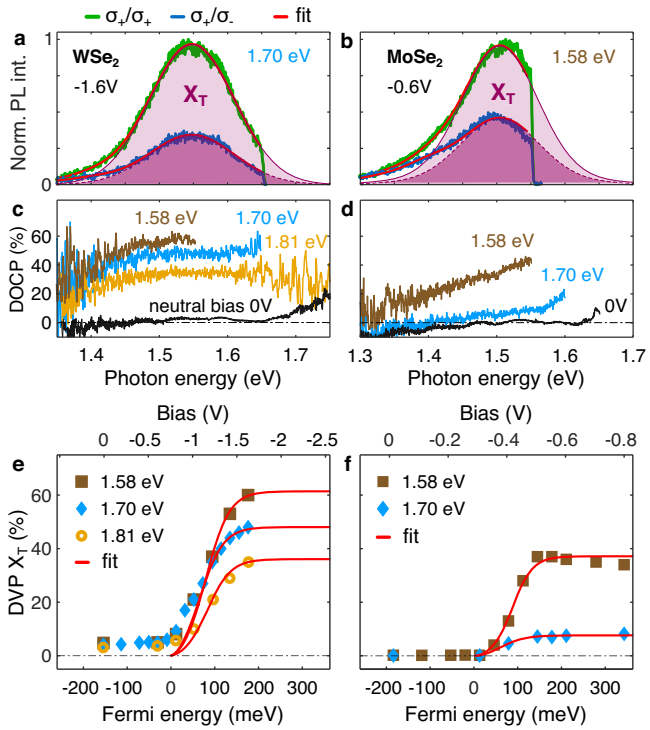

Fig. 4 | Inducing valley polarization in strongly doped TMD monolayers. **a**, **b** Polarization-resolved spectra acquired at negative bias and near-resonance excitation, where the green and blue lines correspond to the co- (σ_+/σ_+) and cross-polarized (σ_+/σ_-) detection channels, the purple-shaded peaks represent the trion contribution obtained from the spectral decomposition fit. We extract DVP values in panels a 48% and b 36%. **c**, **d** Corresponding DOCP at neutral (black) and negative (colored curves) bias, where colors correspond to the laser excitation energy. **e**, **f** Evolution of the trion valley polarization in the emission of WSe_2 and $MoSe_2$ monolayers at on- and off-resonant excitation. The transition to high valley polarization is fitted with Eq. (3) (red).

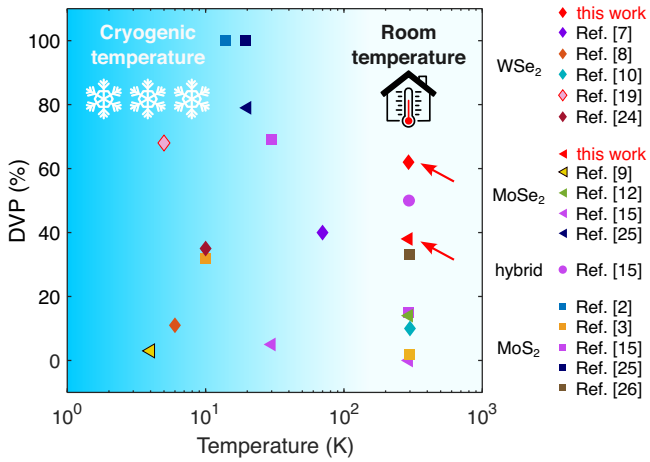

Fig. 5 | Valley polarization of TMD monolayers at cryogenic and room temperature. Values obtained for WSe_2 and $MoSe_2$ monolayers in this work are highlighted in red color. Data points for WSe_2 (♦), $MoSe_2$ (◄), MoS_2 (▪), and hybrid monolayers $Mo(S_{0.8}Se_{0.2})_2$ (•), are taken from references shown in the inset, where the same color corresponds to the same reference.

electrochemical cell design needs optimization to ensure doping stability and uniformity while preventing Faradaic currents and electrolysis at high voltages. Overdoping risks introducing defects or altering the band structure while also causing irreversible changes to the optoelectronic response of TMD monolayers. We also note that, at high doping levels, the interaction between trions and the lattice could lead to a transition where the trion state evolves into a polaron state forming polaronic trions[23] thereby introducing an additional toolkit for controlling optoelectronic and valleytronic properties of TMD monolayers.

In summary, we investigated valley polarization in WSe_2 and $MoSe_2$ monolayers under strong electron doping at room temperature. We achieved high trion DVP values of 61% and 37% in WSe_2 and $MoSe_2$ monolayers, respectively, under doping concentrations of over 10^{13} cm^{-2}. The strong-doping regime allows for controlling the characteristic times of emission and intervalley scattering processes, which prevents the intervalley scattering and induces the high valley polarization even at room temperature. Our results demonstrate the importance of developing robust charge doping techniques to realize the strong-doping regime in TMD monolayers to enable the high valley polarization for practical valleytronic applications at room temperature.

Data availability

The datasets used and/or analyzed during the current study are available from the corresponding author on reasonable request.

Received: 3 October 2023; Accepted: 1 March 2024;
Published online: 20 March 2024

References

1. Liu, Y. et al. Valleytronics in transition metal dichalcogenides materials. *Nano Res.* **12**, 2695–2711 (2019).
2. Mak, K. F., He, K., Shan, J. & Heinz, T. F. Control of valley polarization in monolayer MoS_2 by optical helicity. *Nat. Nanotechnol.* **7**, 494–498 (2012).
3. Zeng, H., Dai, J., Yao, W., Xiao, D. & Cui, X. Valley polarization in MoS_2 monolayers by optical pumping. *Nat. Nanotechnol.* **7**, 490–493 (2012).
4. Jones, A. M. et al. Optical generation of excitonic valley coherence in monolayer WSe_2. *Nat. Nanotechnol.* **8**, 634–638 (2013).
5. Feng, S. et al. Engineering valley polarization of monolayer WS_2: a physical doping approach. *Small* **15**, 1805503 (2019).
6. Lundt, N. et al. Optical valley hall effect for highly valley-coherent exciton-polaritons in an atomically thin semiconductor. *Nat. Nanotechnol.* **14**, 770–775 (2019).
7. Shinokita, K. et al. Continuous control and enhancement of excitonic valley polarization in monolayer WSe_2 by electrostatic doping. *Adv. Funct. Mater.* **29**, 1900260 (2019).
8. Zheng, H. et al. Strain-tunable valley polarization and localized excitons in monolayer WSe_2. *Opt. Lett.* **48**, 2393 (2023).
9. Wang, G. et al. Polarization and time-resolved photoluminescence spectroscopy of excitons in $MoSe_2$ monolayers. *Appl. Phys. Lett.* **106**, 112101 (2015).
10. Yan, Y. et al. Enhancement of valley polarization in monolayer WSe_2 coupled with microsphere-cavity-array. *Adv. Funct. Mater.* **33**, 2213933 (2023).
11. Lin, W.-H. et al. Electrically tunable and dramatically enhanced valley-polarized emission of monolayer WS_2 at room temperature with plasmonic archimedes spiral nanostructures. *Adv. Mater.* **34**, 2104863 (2021).
12. Lorchat, E. et al. Room-temperature valley polarization and coherence in transition metal dichalcogenide-graphene van der Waals heterostructures. *ACS Photonics* **5**, 5047–5054 (2018).
13. Konabe, S. Screening effects due to carrier doping on valley relaxation in transition metal dichalcogenide monolayers. *Appl. Phys. Lett.* **109**, 073104 (2016).
14. Miyauchi, Y. et al. Evidence for line width and carrier screening effects on excitonic valley relaxation in 2D semiconductors. *Nat. Commun.* **9**, 2598 (2018).
15. Liu, S. et al. Room-temperature valley polarization in atomically thin semiconductors via chalcogenide alloying. *ACS Nano* **14**, 9873–9883 (2020).

16. Robert, C. et al. Spin/valley pumping of resident electrons in WSe_2 and WS_2 monolayers. *Nat. Commun.* **12**, 5455 (2021).
17. Morozov, S., Wolff, C. & Mortensen, N. A. Room-temperature low-voltage control of excitonic emission in transition metal dichalcogenide monolayers. *Adv. Opt. Mater.* **9**, 2101305 (2021).
18. Carmiggelt, J. J., Borst, M. & van der Sar, T. Exciton-to-trion conversion as a control mechanism for valley polarization in room-temperature monolayer WS_2. *Sci. Rep.* **10**, 17389 (2020).
19. Oliver, S. M. et al. Valley phenomena in the candidate phase change material $WSe_{2(1-x)}Te_{2x}$. *Commun. Phys.* **3**, 10 (2020).
20. Hao, K. et al. Trion valley coherence in monolayer semiconductors. *2D Mater.* **4**, 025105 (2017).
21. Han, B. et al. Exciton states in monolayer $MoSe_2$ and $MoTe_2$ probed by upconversion spectroscopy. *Phys. Rev. X* **8**, 031073 (2018).
22. Wang, G. et al. Colloquium: Excitons in atomically thin transition metal dichalcogenides. *Rev. Mod. Phys.* **90**, 021001 (2018).
23. Sarkar, S. et al. Polaronic trions at the $MoS_2/SrTiO_3$ interface. *Adv. Mater.* **31**, 1903569 (2019).
24. Hsu, W.-T. et al. Optically initialized robust valleypolarized holes in monolayer WSe_2. *Nat. Commun.* **6**, 8963 (2015).
25. Tornatzky, H., Kaulitz, A.-M. & Maultzsch, J. Resonance profiles of valley polarization in single-layer MoS_2 and $MoSe_2$. *Phys. Rev. Lett.* **121**, 167401 (2018).
26. Wan, Y. et al. Epitaxial single-layer MoS_2 on GaN with enhanced valley helicity. *Adv. Mater.* **30**, 1703888 (2017).

Acknowledgements

We acknowledge stimulating discussions with Vladimir A. Zenin. S.M. acknowledges funding from the Marie Skłodowska-Curie Action (grant No. 101032967). N.A.M. is a VILLUM Investigator supported by VILLUM FONDEN (grant No. 16498). The Center for Polariton-driven Light-Matter Interactions (POLIMA) is funded by the Danish National Research Foundation (Project No. DNRF165).

Author contributions

S.M. conceived the idea and managed the project. S.M. and T.Y. performed the experiments. S.M. and C.W. analyzed the data. S.I.B. and N.A.M. supervised the project. The results were discussed by all authors and the writing of the manuscript was done in a joint effort. All authors provided critical feedback and helped shape the research, analysis, and paper.

Competing interests

The authors declare no competing interests.

Additional information

Supplementary information The online version contains supplementary material available at https://doi.org/10.1038/s41699-024-00459-8.

Correspondence and requests for materials should be addressed to Sergii Morozov.